Volume 5
Number 3
March 2026
Pages 243–366

Energy Advances

rsc.li/energy-advances

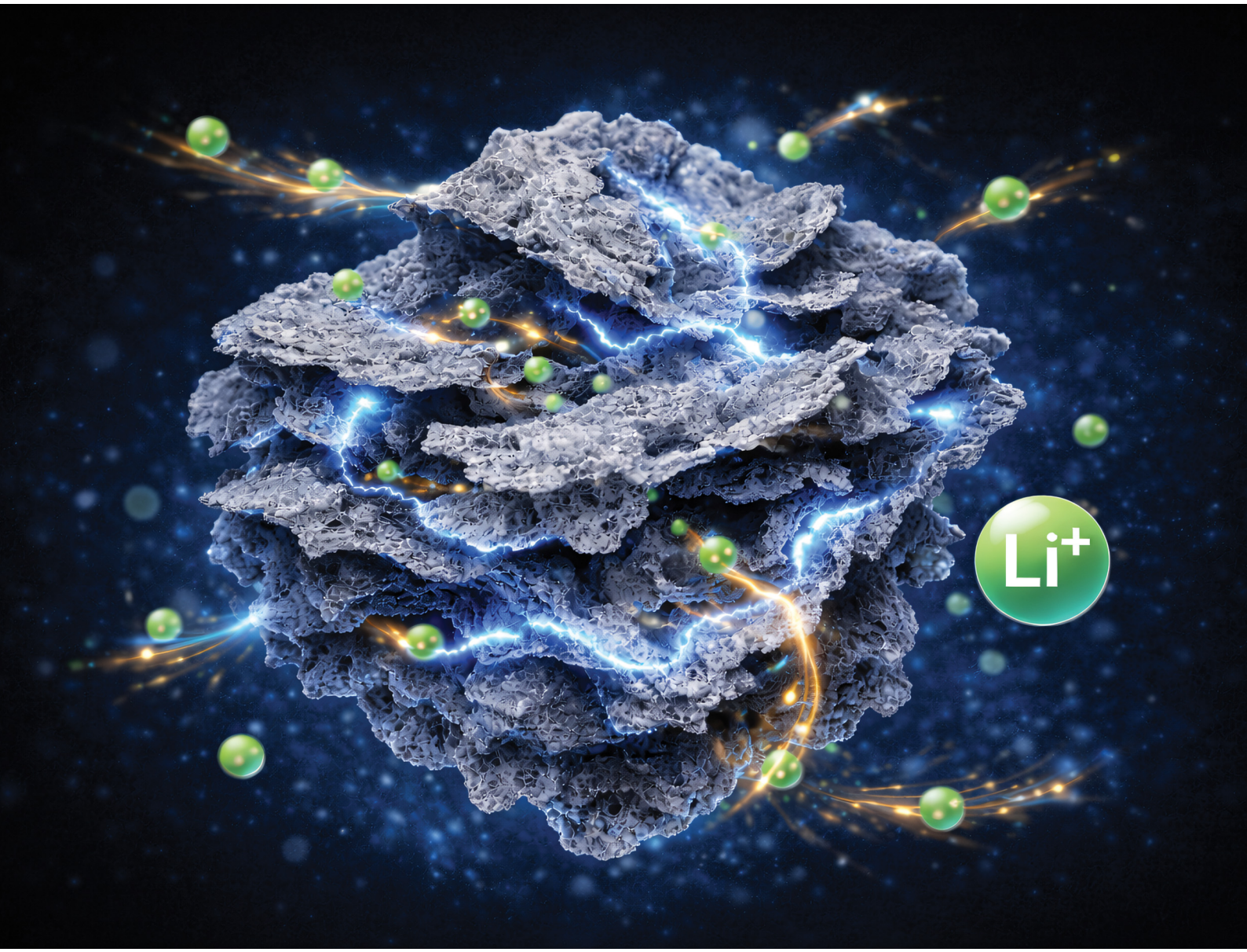

ISSN 2753-1457

ROYAL SOCIETY OF CHEMISTRY

COMMUNICATION
Michael Naguib *et al.*
High-power two-dimensional molybdenum boride MBene electrodes for lithium-ion batteries and capacitors

Energy Advances

ROYAL SOCIETY OF CHEMISTRY

COMMUNICATION

View Article Online
View Journal | View Issue

Cite this: *Energy Adv.*, 2026, 5, 263

Received 12th October 2025,
Accepted 23rd January 2026

DOI: 10.1039/d5ya00295h

rsc.li/energy-advances

High-power two-dimensional molybdenum boride MBene electrodes for lithium-ion batteries and capacitors

Karamullah Eisawi,[a] Connor J. Herring,[b] Jean G. A. Ruthes,[cd] Volker Presser,[cde] Matthew M. Montemore[b] and Michael Naguib *[a]

There is a need for new electrochemical energy storage materials that can handle high cycling rates (high power) for rapid charging without compromising high energy density, such as high-power Li-ion batteries (LIBs) and Li-ion capacitors (LICs). Electrically conductive and redox-active two-dimensional (2D) materials, such as transition metal carbides and borides, are promising candidates for these applications. Tailoring in-plane chemically ordered MAB phases (*i*-MAB) has facilitated the synthesis of their 2D derivatives (*i*-MBenes), which possess ordered vacancies at the metal sites. The first reported *i*-MBene paper is $Mo_{4/3}B_2T_x$, which is derived from the parent *i*-MAB phase $(Mo_{2/3}Y_{1/3})_2AlB_2$ by the selective etching of Al and Y. In this study, we report on the synthesis of 2D $Mo_{4/3}B_2T_x$ aerogel and its electrochemical performance as an electrode material for LIBs. Our aerogel exhibits remarkable stability during life-cycling testing at high applied specific currents, maintaining a specific capacity of 260 mAh g^{-1} even after completing 500 cycles under a high specific current of 2 A g^{-1}. At a moderate specific current of 100 mA g^{-1}, it delivers an energy density of 363 Wh kg^{-1}, while at a high specific current of 2 A g^{-1}, it achieves a specific power of 1300 W kg^{-1}. Complementary density functional theory calculations further reveal that Li preferentially occupies hexagonal Mo sites in $Mo_{4/3}B_2T_x$, supporting the observed stable lithiation behavior and excellent high-rate capability. These results suggest that 2D $Mo_{4/3}B_2T_x$ aerogel is a promising candidate for high-power LIBs and LICs.

1. Introduction

Electrochemical energy storage[1] has become an integral part of daily life across various fields. Specifically, lithium-ion batteries (LIBs) have become the primary storage technology for mobile and, increasingly, stationary applications due to their high reversible capacity, large-scale availability, and decreasing costs.[2–4] However, the growing demand for advanced energy storage solutions necessitates extensive research to enhance energy density while maintaining long cycle life.[5,6] Lithium-ion capacitors (LICs) have been introduced as hybrid electrochemical storage systems that combine the high energy storage capacity and long cycle life from LIBs with the high power density from supercapacitors.[7–9]

Two-dimensional (2D) materials are promising for storing lithium as they possess high surface area, fast ion transport and effective dendrite suppression, making them well-suited for use as anode materials.[10–12] Specifically, MXenes are an emerging class of 2D materials derived by selectively etching out A-group elements from the parent MAX phase, typically represented by the formula $M_{n+1}AX_n$, to form the formula $M_{n+1}X_nT_x$.[13] In these notations, M stands for early transition metals (*e.g.*, Ti, Nb, V, Mo) and A denotes A-group elements (*e.g.*, Al, Ga, Si), while X refers to carbon or nitrogen. The surface terminations, denoted as T_x, can include groups like fluorine (–F), oxygen (–O), chlorine (–Cl), and hydroxyl (–OH). These materials are highly attractive for energy storage applications due to their high electrical conductivity,[14,15] tunable interlayer spacing that facilitates ion diffusion,[16–18] large surface area, and customizable surface terminations.[19,20] Analogous to MXenes, MBenes represent a newly discovered class of 2D materials, in which the X sites are occupied by boron.[21,22] Computational studies have predicted their potential for energy storage applications, suggesting promising electrochemical performance.[23–25] Despite the difficulty in fully etching out Al from MoAlB MAB, our previous study indicated that the partially etched Mo_2AlB_2 phase could be a promising anode material for LIBs, exhibiting a specific capacity of 156 mAh g^{-1} after 500 cycles at a rate of 500 mA g^{-1}. Furthermore, milling Mo_2AlB_2 significantly enhanced its electrochemical performance, achieving a specific capacity of 283 mAh g^{-1}.[26] The introduction of vacancies in MBenes was achieved by first

[a] *Department of Physics and Engineering Physics, Tulane University, New Orleans, LA 70118, USA. E-mail: naguib@tulane.edu*
[b] *Department of Chemical and Biomolecular Engineering, Tulane University, New Orleans, LA 70118, USA*
[c] *INM – Leibniz Institute for New Materials, D2 2, 66123, Saarbrücken, Germany*
[d] *Department of Materials Science & Engineering, Saarland University Campus D2 2, 66123, Saarbrücken, Germany*
[e] *saarene, Saarland Center for Energy Materials and Sustainability, Campus C4 2, 66123 Saarbrücken, Germany*

inducing in-plane chemical ordering within MAB phases, known as *i*-MAB phases, which follow the general formula $(M'_{2/3}M''_{1/3})_2AlB_2$. The first reported *i*-MBene, $Mo_{4/3}B_2T_x$, was derived from the parent *i*-MAB phase $(Mo_{2/3}Y_{1/3})_2AlB_2$ by the selective etching of Al and Y.[27]

Recent studies highlight the promising role of $Mo_{4/3}B_2T_x$ in various battery systems. As an anode in LIBs, multilayers of $Mo_{4/3}B_2T_x$ offer a specific capacity of nearly 280 mAh g^{-1} after 100 cycles at a specific current of 50 mA g^{-1}.[28] In sodium-ion batteries (SIBs), its combination with MoS_2 enhances ion transport, achieving 267 mAh g^{-1} after 600 cycles at 2 A g^{-1}.[29] $Mo_{4/3}B_2T_x$ also serves as an effective iodine host in Zn-I_2 batteries, maintaining 107 mAh g^{-1} at 25 A g^{-1} for extreme cycling life up to 230 000 cycles.[30] As for lithium–oxygen (Li–O_2) batteries, the fabricated superlattice between $Mo_{4/3}B_2T_x$ and $Ti_3C_2T_x$ with enhanced oxygen redox reactions has led to a high discharge specific capacity of 17 000 mAh g^{-1} and a cycling life of 475 cycles at 300 mA g^{-1}.[31]

However, previous LIB studies on $Mo_{4/3}B_2T_x$ have only examined multilayered structures, leaving the performance of delaminated 2D $Mo_{4/3}B_2T_x$ largely unexplored.[28] Moreover, these studies were limited to relatively low applied currents and short cycle life. Herein, we explored, for the first time, the application of $Mo_{4/3}B_2T_x$ in LIBs using delaminated material (Fig. 1), which offers better accessibility to electrochemically active sites for Li storage. To better understand its behavior, we also carried out density functional theory (DFT) calculations, which revealed that Li insertion is most favorable at the hexagonal Mo site. This atomic-level insight helps explain the stable solid-solution lithiation mechanism. Extending electrochemical testing to higher current densities and long-term cycling, our aerogel structure exhibits high cycling stability, maintaining a specific capacity of about 260 mAh g^{-1} even after 500 cycles at 2 A g^{-1}, which far exceeds previously reported values. By leveraging the high stability of 2D $Mo_{4/3}B_2T_x$ at a high applied specific current, this work offers a promising anode material for both LIBs and LICs.

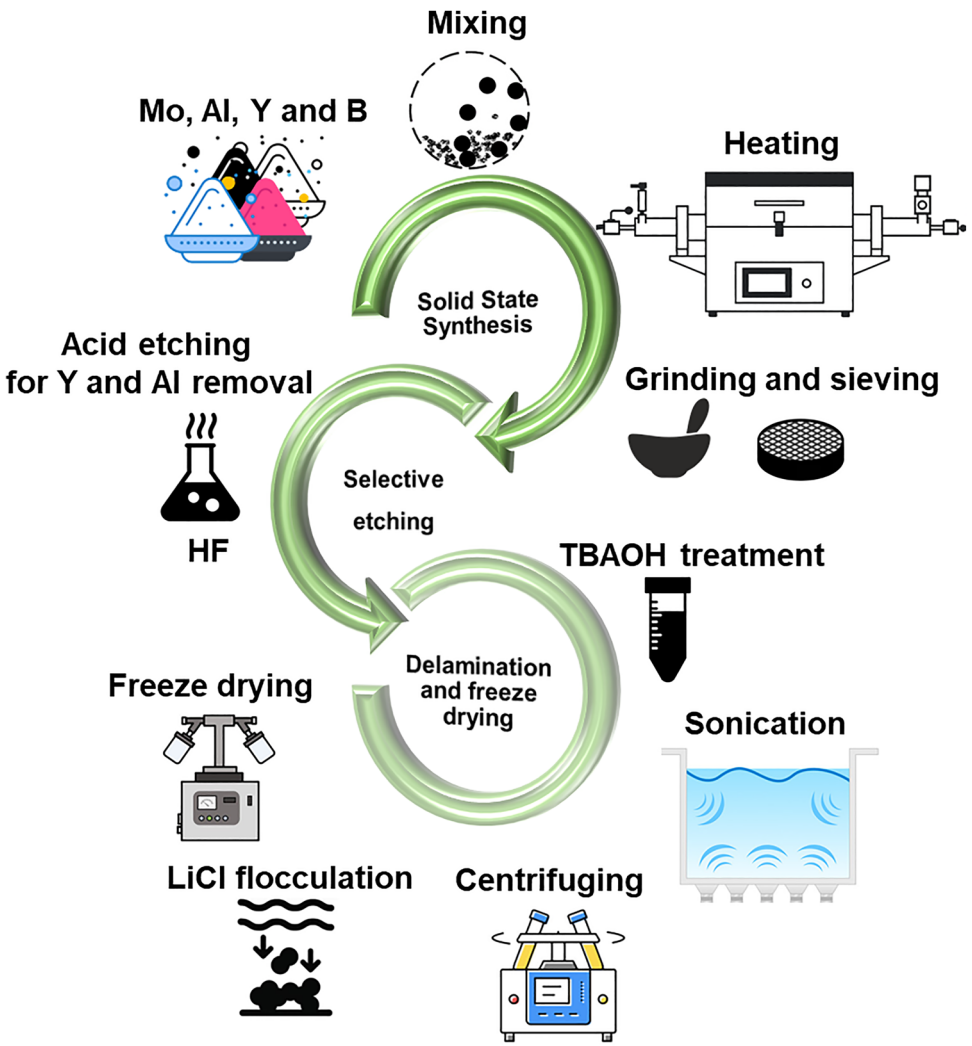

Fig. 1 Schematic of the procedure: starting with the solid-state synthesis of $Mo_{4/3}Y_{2/3}AlB_2$ *i*-MAB phase, followed by selective etching to produce $Mo_{4/3}B_2T_x$ *i*-MBene, and concluding with the preparation of aerogel.

2. Experimental work

2.1. Synthesis of $Mo_{4/3}Y_{2/3}AlB_2$ *i*-MAB phase and $Mo_{4/3}B_2T_x$ *i*-MBene

A schematic for the material synthesis is shown in Fig. 1. $Mo_{4/3}Y_{2/3}AlB_2$ was prepared from molybdenum (Mo, -250 mesh, 99.9%, Thermo Scientific), aluminum (Al, -325 mesh, 99.5%, Thermo Scientific), yttrium (Y, -40 mesh, 99.6%, Alfa Aesar) and boron (B, -325 mesh, 98%, Alfa Aesar). The powders were combined in a molar ratio of Mo : Y : Al : B equal to 1.33 : 0.67 : 1.10 : 2.00. To ensure homogeneity, the mixture was loaded with 10 mm yttria-stabilized zirconia balls and blended in a mixer (Turbula T2F) at 56 rpm for 3 h. The mixture was then placed in an alumina crucible positioned at the center of a tube furnace. The sample was heated under flowing argon (0.2 L min^{-1}) at a rate of 5 °C min^{-1} to 1400 °C with a holding time of 8 h. After heating, the resulting $Mo_{4/3}Y_{2/3}AlB_2$ brick was left inside the furnace to cool under Ar. Afterwards, the sample was crushed and sieved to achieve particle sizes below 45 μm.

For the synthesis of $Mo_{4/3}B_2T_x$, selective etching of aluminum and yttrium from $Mo_{4/3}Y_{2/3}AlB_2$ was performed using hydrofluoric acid (HF, 50% solution in water, Thermo Scientific). The etchant volume was 10 mL per 1 g of $Mo_{4/3}Y_{2/3}AlB_2$. The powder was slowly introduced to the etchant under magnetic stirring at 500 rpm and 35 °C for 24 h. After etching, the resulting suspension was divided into 50 mL centrifuge tubes, using one tube for every 0.5 g of the precursor powder. The product was washed with deionized water through repeated centrifugation at 3500 rpm for 2 min, discarding the supernatant each time. The sediments were then redispersed in fresh DI water using a vortex mixer. This washing cycle continued until the pH of the supernatant reached ~6.

2.2. Delamination of $Mo_{4/3}B_2T_x$ *i*-MBene and aerogel fabrication

The washed $Mo_{4/3}B_2T_x$ was soaked in 20 mass% aqueous tetrabutylammonium hydroxide (TBAOH, 99%, Thermo Scientific) using a ratio of 10 mL solution per 1 g of the precursor powder for 15 min at room temperature in a 50 mL centrifuge tube. After soaking, the suspension was centrifuged at 5000 rpm for 25 min to remove excess TBAOH, and the supernatant was decanted. Residual TBAOH was eliminated by four sequential ethanol rinsing and centrifuging at 5000 rpm for 5 min, with the supernatant discarded after each cycle. After the ethanol wash, deionized water was added to the sample, and the sediment was redispersed and sonicated for 1 h in an ultrasonic water bath maintained at 10 °C and operated at 37 kHz. Following sonication, the sample was centrifuged at 2500 rpm for 30 min. The resulting colloidal solution was collected and flocculated by treating it with a 15 M lithium chloride solution (LiCl, 99%, Thermo Scientific) for 2 h. This step was performed to exchange any residual TBA^+ ions with Li^+, thereby minimizing degradation.[32] After flocculation, the sample was washed with deionized water by centrifuging at 3500 rpm for 3 min. This washing cycle continued until a pH of 5 was reached. Finally, the sample was freeze-dried at −50 °C for 72 h to obtain the $Mo_{4/3}B_2T_x$ aerogel.

2.3. Materials characterization

X-ray diffraction (XRD) patterns were obtained using a Rigaku D/Max-2200 powder diffractometer, employing a step size of 0.02° and a scan rate of 1° min^{-1}, using Cu Kα radiation at 40 mA and 40 kV. Powders were spread evenly on a low-background sample holder. Scanning electron microscopy (SEM) micrographs were collected with a Hitachi S-4800 operated at 3 kV. Samples were mounted on an aluminum stub using conductive carbon tape. Elemental composition was analyzed with a Hitachi S-3400 SEM coupled to an Oxford energy-dispersive X-ray spectroscopy (EDS) detector operated at 30 kV. Transmission electron microscopy (TEM) samples were prepared by diluting 1 mL of the colloidal solution and drop-casting onto a copper grid coated with lacey carbon. TEM micrographs were obtained using an FEI Tecnai G2-F30 transmission electron microscope operated at 300 kV.

Attenuated total reflectance Fourier transform infrared (ATR-FTIR) measurements were conducted using a Bruker Vertex 70 FT-IR spectrometer equipped with an attenuated total reflectance apparatus, exploring a spectral range from 400 cm^{-1} to 4000 cm^{-1} with a resolution of 4 cm^{-1} under 256 scans. Before each measurement, a background spectrum was collected, accounting for atmospheric absorption and instrumental drift. The samples were dried at 80 °C under vacuum for 8 h prior to the analysis to minimize moisture. Raman spectroscopy was conducted using a Renishaw inVia Raman microscope, which employed a Nd:YAG laser with an excitation wavelength of 532 nm and a power of 799 μW at the focal point of the sample with a numerical aperture of 0.75. Before the measurements, a silicon standard was used for calibrating the system. For each sample, spectra from 3 points were recorded with a 10 s exposure time and accumulated five times. Samples were prepared by placing them on a glass slide. Spectra were treated by cosmic ray removal.

2.4. Electrode preparation and electrochemical measurements

LIB testing was conducted to investigate the electrochemical properties of $Mo_{4/3}B_2T_x$. Electrode slurries were prepared by blending $Mo_{4/3}B_2T_x$ with carbon black (CB, Alfa Aesar, >99.9%) and polyvinylidene fluoride (PVDF, molecular weight ≈ 534 000, Sigma-Aldrich) dissolved in *N*-methyl-2-pyrrolidinone (99.5%, Acros Organics, extra dry over molecular sieve). A mass ratio of 8 : 1 : 1 for $Mo_{4/3}B_2T_x$: CB : PVDF was maintained. The slurry was drop-cast onto 25 μm thick copper foil, which served as the current collector, and dried at 60 °C for 48 h to obtain working electrodes. The mass loading of the $Mo_{4/3}B_2T_x$ active material was approximately 0.8-0.9 mg cm^{-2} and electrode thickness was ~30 μm. Cell assembly was performed in an Ar-filled glove box with H_2O and O_2 levels below 1 ppm. CR2032 coin cells were fabricated using $Mo_{4/3}B_2T_x$ as the working electrode, metallic Li as counter and reference electrodes. The electrolyte was 1 M $LiPF_6$ in a 3 : 7 mixture of ethylene carbonate (EC) and ethyl methyl carbonate (EMC) with a glass fiber separator. Potentiostatic electrochemical impedance spectroscopy (PEIS) and

Cyclic voltammetry (CV) were conducted on a BioLogic VMP3 electrochemical workstation. PEIS was conducted at frequencies ranging from 300 kHz to 100 mHz with an amplitude of 30 mV, while CV was carried out in a voltage window of 1 mV to 3 V *vs.* Li/Li^+. Additionally, galvanostatic cycling and rate capability tests were performed in the same voltage range at specific currents from 20 mA g^{-1} to 2 A g^{-1} using a Landt CT2001A cycler.

2.5. Computational methods

Density functional theory (DFT) calculations were conducted using the Vienna *Ab Initio* Simulation Package (VASP)[33,34] with the Perdew–Burke–Ernzerhof (PBE)[35] generalized gradient exchange–correlation functional. A cutoff energy of 400 eV was used for all calculations in this study. The unit cell consisted of a bottom and top layer of 8 Mo atoms, with 24 B atoms sandwiched between a 24 Å vacuum gap set along the z direction. O-terminated structures were the primary focus of this study, with 12 O atoms bound to both the top and bottom Mo layers. For all calculations, a 7 × 8 × 1 Monkhorst–Pack *k*-point mesh was used. Relaxations were run until residual forces were less than 0.03 eV $Å^{-1}$, and the self-consistent field loop used an energy convergence of 10^{-4} eV. The lattice constant for the relaxed $Mo_{4/3}B_2$ structure was 5.17 Å, in agreement with other computational work.[36] Upon O-termination, this value increased to 5.24 Å.

The addition of Li was studied by relaxing the structures with Li added either atop a Mo atom, on a Mo–Mo bridge site, or within the hexagonal Mo ring, designated as a hexagon. A transition state was also found with the dimer method, between the top and bridge sites.[37] From the energy of these states, the Li intercalation energy and diffusion barrier were calculated. The intercalation energy was defined as the difference between the total energy of the system with the Li atom adsorbed on the surface and the sum of the energies of the clean surface and Li in the bulk phase. The Li diffusion barrier was calculated as the difference in energy between the lowest energy geometry and the transition state. A vibrational frequency calculation was performed to verify the transition state.

3. Results and discussion

3.1. Materials characterization

The successful synthesis of $Mo_{4/3}Y_{2/3}AlB_2$ was confirmed using XRD (Fig. 2a) and SEM (Fig. 2b). X-ray diffractograms of the as-synthesized sample show reflections at 11.73°, 23.53°, 32.87°, and 40.84° 2θ, corresponding to the (003), (006), (110), and (116) planes of $Mo_{4/3}Y_{2/3}AlB_2$, respectively.[27] The SEM micrograph of $Mo_{4/3}Y_{2/3}AlB_2$ reveals a layered morphology for the intended phase that is typical for layered ceramics.

As shown in Fig. 2a, after etching, the X-ray diffractogram of the multilayered $Mo_{4/3}B_2T_x$ reveals an additional low-angle (00*l*) peak at 9.49° 2θ, a feature frequently reported following selective etching of MAX phases.[38] After delamination, $Mo_{4/3}B_2T_x$ aerogel exhibits a much broader (00*l*) reflection at ~6.5° 2θ. The significant broadening and shifting to a lower angle reflect the exfoliation and formation of a less ordered structure typical of aerogels. The scanning electron micrograph in Fig. 2c shows the morphology of $Mo_{4/3}B_2T_x$ aerogel, indicating successful delamination and subsequent freeze-drying by displaying an interconnected network of fluffy nanosheets. The elemental composition of $Mo_{4/3}B_2T_x$ aerogel, determined by EDS, is provided in SI, Table S1. The EDS analysis confirms the selective etching and removal of both Al and Y.

The TEM micrograph in Fig. 2d displays the morphology of 2D $Mo_{4/3}B_2T_x$ sheets. The inset shows the selected area electron diffraction (SAED) pattern, which reveals a clear hexagonal lattice structure aligned with the expected structure, further validating the successful delamination of $Mo_{4/3}B_2T_x$.

ATR-FTIR spectroscopy was used to evaluate the removal of TBA^+ with the LiCl treatment. The spectra shown in Fig. S1 for the TBAOH delaminated $Mo_{4/3}B_2T_x$ aerogel display defined signals from 500–1250 cm^{-1}, which are characteristic bands associated with skeletal motion of TBA^+, along with asymmetric bending (δCH_2) and stretching vibrations (νCH_3) signals from 1360–1500 cm^{-1}.[39] However, the characteristic bands associated with TBA^+ after the LiCl treatment were significantly minimized, suggesting the success in the removal of this molecule. Additionally, the remaining distinct signals are associated with both *i*-MAB and its derived *i*-MBene, presenting two characteristic modes associated with the boron in the bulk of the particles. The broad signal centered at 1066 cm^{-1} corresponds to an asymmetric stretching (ν_{B-B}) of B–B which suggests a 2D arrangement of boron.[40] The sharp bands present at 2848 cm^{-1}, 2916 cm^{-1} and 3672 cm^{-1} are characteristic bands of B-B vibrations ($\beta_{(B-B)}$) in a 2D borophene-like conformation.[41,42] Furthermore, borate-related vibrational features were observed in both the *i*-MAB phase and its corresponding *i*-MBene. The bands located at 719 cm^{-1} and 1474 cm^{-1} are consistent with B–O–B bending and B–O stretching vibrations, respectively.[43,44] These results confirm the efficient removal of TBA^+ with the LiCl treatment. Raman spectroscopy was performed to further assess the impact of the LiCl in the removal of TBA^+. The spectra shown in Fig. S2 also indicate successful removal, as we can observe the bands at 1316 and 1454 cm^{-1} associated with the bending modes of CH_2 disappearing after the LiCl treatment.[45,46] The characteristic MoB nanosheet bands at 205 and 288 cm^{-1} present in all samples associated with the E_{1g} and A_{1g} transitions of boron, along with bands present at 820 cm^{-1} related to the vibrations of Mo–B, and 958 and 985 cm^{-1} bands associated with B–B vibrations further confirm the extraction of Al.[46–48]

3.2. Electrochemical performance for $Mo_{4/3}B_2T_x$ as an electrode for LIBs

Electrochemical testing of $Mo_{4/3}B_2T_x$ as electrode materials for LIBs was carried out in coin cell configuration. CV was performed at scan rates of 0.1 mV s^{-1}, 0.2 mV s^{-1}, 0.5 mV s^{-1}, 1.0 mV s^{-1}, and 2.0 mV s^{-1} (Fig. 3a). As the scan rate increased, the sharp redox peaks were broadened and shifted,[49] suggesting a kinetic limitation for ionic diffusion.[50] This behavior is common for non-diffusion-controlled materials.[51] The inset in Fig. 3a shows the *b*-value *versus* log(ν). The *b*-value is a crucial

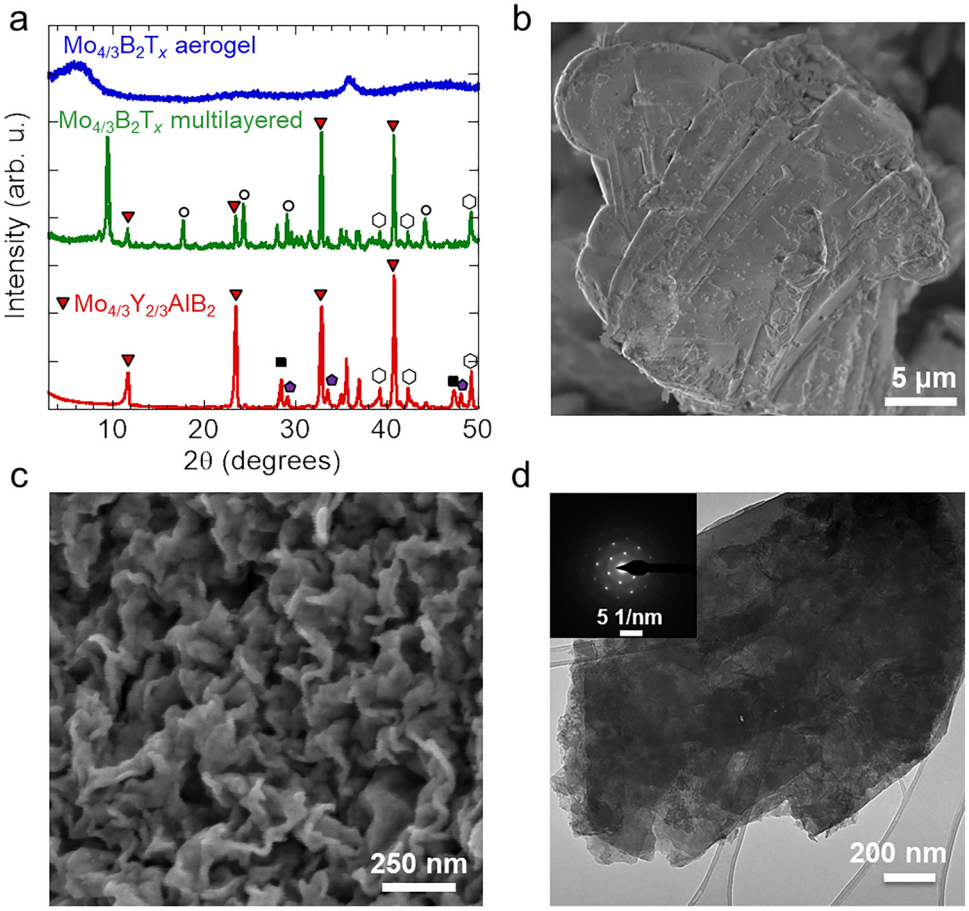

Fig. 2 Characterization of $Mo_{4/3}Y_{2/3}AlB_2$ *i*-MAB phase, $Mo_{4/3}B_2T_x$ *i*-MBene multilayered and $Mo_{4/3}B_2T_x$ *i*-MBene aerogel. (a) X-ray diffractograms for $Mo_{4/3}Y_{2/3}AlB_2$, $Mo_{4/3}B_2T_x$ *i*-MBene multilayered and $Mo_{4/3}B_2T_x$ aerogel. The peaks marked by ■ indicate Si, used as reference, ⬟ indicate Y_2O_3 (PDF#25-1200), ⬡ indicate MoB (PDF# 00-051-0940), and ○ indicate AlF_3 (PDF#84-1672). (b) Scanning electron micrograph of $Mo_{4/3}Y_{2/3}AlB_2$ *i*-MAB phase. (c) Scanning electron micrograph for $Mo_{4/3}B_2T_x$ *i*-MBene aerogel. (d) Transmission electron micrograph of 2D $Mo_{4/3}B_2T_x$ sheets. Inset: Selected area electron diffraction pattern for these sheets.

parameter in electrochemical analysis that helps determine whether the current response of an electrode material is controlled by diffusion processes or surface (capacitive) processes. It is derived from cyclic voltammograms by plotting the peak current (i_p) against the scan rate (v) in a log–log plot and fitting the data to the equation $i_p = av^b$. *b*-values shifting from 0.5 to 1 indicate a transition from diffusion-controlled responses (battery systems) to non-diffusion-controlled (capacitive and pseudocapacitive systems) responses, respectively.[52] The linear fitting was constructed by recording the anodic peak for each scan rate in the voltammograms. After fitting a linear relationship, the *b*-value for $Mo_{4/3}B_2T_x$ aerogel was found to be 0.87, which indicates a predominant contribution of surface-controlled processes, along with a minor contribution from a diffusion-controlled contribution suggesting a pseudocapacitive mechanism.[53] Therefore, the electrochemical reactions consist of reversible faradaic reaction at the near-surface region, while displaying a capacitive behavior simultaneously.[54,55] Comparing the behavior of $Mo_{4/3}B_2T_x$ with that of partially etched layered molybdenum aluminum boride, *i.e.*, Mo_2AlB_2 synthesized by partially etching Al from MoAlB as reported by Majed *et al.*,[56] will shed light on the different mechanisms governing these similar material systems. The non-diffusion contribution is slightly higher than that observed in the partially etched MAB phase Mo_2AlB_2, which exhibited a *b*-value of 0.7. For comparison, MoO_2-MoO_3 systems showed a *b*-value of 0.75, reflecting a balanced contribution from both surface-controlled and diffusion-controlled mechanisms.[57]

Potentiostatic electrochemical impedance spectroscopy (PEIS) of Mo_2AlB_2 and $Mo_{4/3}B_2T_x$ aerogel was analyzed at open-circuit potential (3.1 and 2.8 V *vs.* Li/Li^+ for Mo_2AlB_2 and $Mo_{4/3}B_2T_x$, respectively) and presented in Fig. 3b. The Nyquist plots highlight the distinct electrochemical behavior of the Mo_2AlB_2 and the $Mo_{4/3}B_2T_x$ aerogel in the low frequency range, indicating a lower diffusion resistance of the aerogel. Consequently, the different materials were investigated through different equivalent circuit analyses shown in Fig. 3b. The circuit elements related to the high-frequency range were equal for both materials, where we employed an equivalent series resistance (ESR), charge-transfer resistance (R_{CT}) in parallel with a constant phase element related to the electrical double layer (Q_{DL}). Since the behavior between materials diverges in the low-frequency

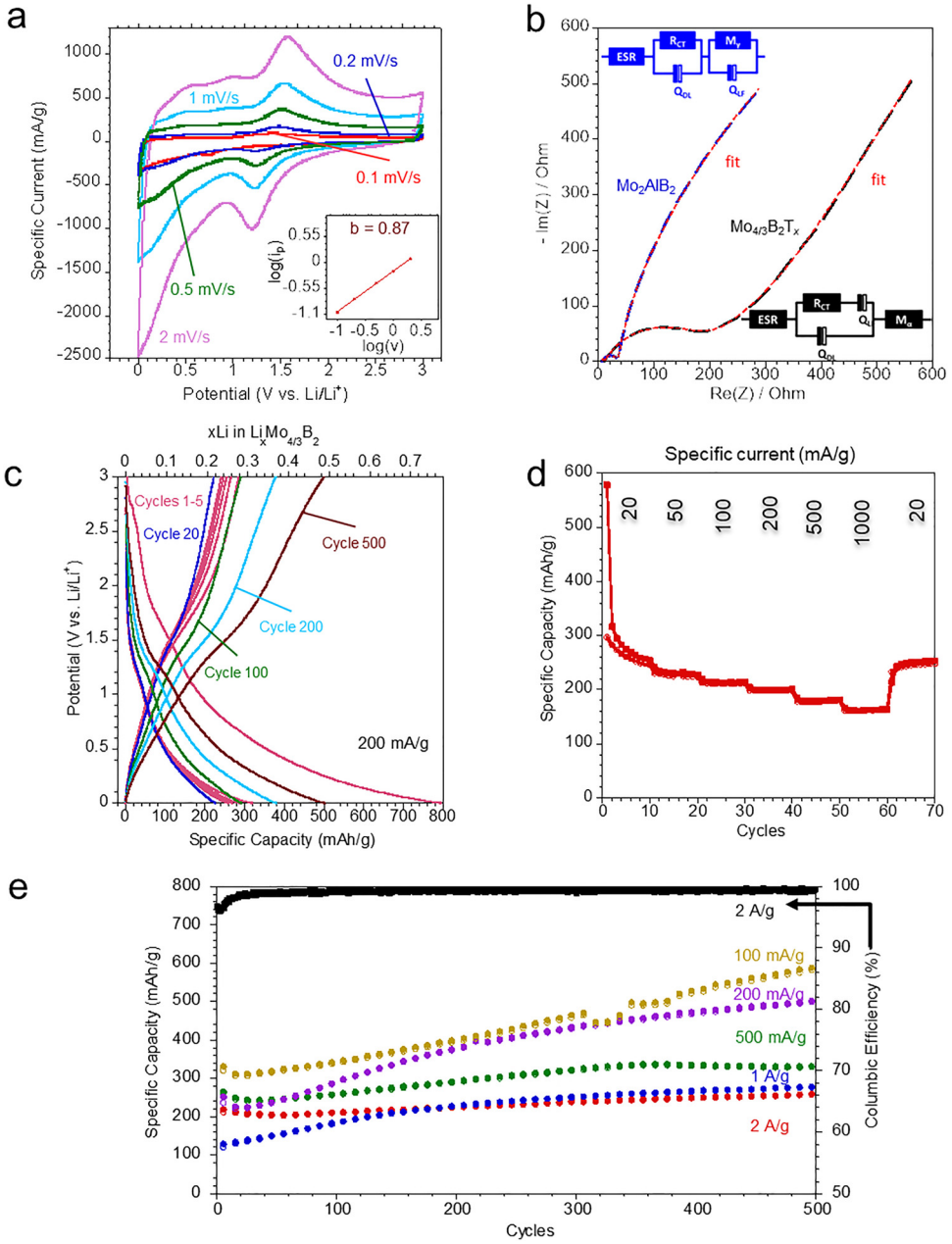

Fig. 3 Electrochemical analysis. (a) Cyclic voltammetry of $Mo_{4/3}B_2T_x$ aerogel at scan rates of 0.1 mV s^{-1}, 0.2 mV s^{-1}, 0.5 mV s^{-1}, 1 mV s^{-1}, and 2 mV s^{-1}. Inset: *b*-value log(i_p)–log(v) plot of voltammograms of $Mo_{4/3}B_2T_x$ aerogel tested at scan rates 0.1–2.0 mV s^{-1}. (b) Potentiostatic electrochemical impedance spectroscopy (PEIS) of $Mo_{4/3}B_2T_x$ aerogel. Inset: Circuit used in fitting the PEIS data where R_s is system resistance, R_{ct} is charge transfer resistance, CPE is a constant phase element, and M_a is a modified, restricted diffusion. (c) Voltage profile of $Mo_{4/3}B_2T_x$ aerogel for cycles 1 to 5, 20, 200, and 500 at 200 mA g^{-1}. (d) Rate handling capability of $Mo_{4/3}B_2T_x$ aerogel at specific currents ranging from 20 mA g^{-1} to 1000 mA g^{-1}. (e) Cycling stability of $Mo_{4/3}B_2T_x$ aerogel at 100 mA g^{-1}, 200 mA g^{-1}, 1000 mA g^{-1}, and 2000 mA g^{-1} along with the Coulombic efficiency at 2000 mA g^{-1}.

range, we employed a second constant phase element representing the charge intercalation (Q_{LF}) in series with a modified restricted diffusion element (M_α) in the aerogel, and in parallel with an anomalous diffusion element (M_γ) in the Mo_2AlB_2. The fitted values are shown in SI, Table S4. There is a noticeable discrepancy in the R_{CT} values as Mo_2AlB_2 showed 29.25 Ω while the aerogel displayed a significantly higher value of 168.4 Ω. This deviation may be associated with the distinct morphology of the aerogel, which undergoes delamination, revealing new electroactive sites present in the vacancies at the Mo-lattice sites, occluding the charge-carriers and potentially hindering ionic mobility due to electrostatic interactions.[58–61] This is further supported by the deviation in the Q_{DL} values, as Mo_2AlB_2 exhibited 41 μF $s^{(n-1)}$ while $Mo_{4/3}B_2T_x$ exhibited 39 μF $s^{(n-1)}$, although the aerogel electrode suggested a more inhomogeneous surface in comparison with Mo_2AlB_2, as indicated by the n_{DL} values of 0.706 and 0.760 respectively.[62] The most significant distinction in the materials can be observed in the low-

frequency range, where the aerogel indicated a higher Q_{LF} capacitance value of 3.5 mF $s^{(n-1)}$ with n_{LF} of 0.591 compared to the 0.8 mF $s^{(n-1)}$ with n_{LF} of 0.323 of the Mo_2AlB_2 electrode. These values suggest an improved ion accessibility to electroactive sites in the aerogel, which is further supported by the broadening of the redox peaks with increasing scan-rates, as shown in Fig. 3a.[61,62] Still in the low frequency range, Mo_2AlB_2 indicated an anomalous diffusion behavior while $Mo_{4/3}B_2T_x$ a restricted behavior, given the deviation of n_{LF} factor. From the equivalent circuit analysis, the $Mo_{4/3}B_2T_x$ aerogel displayed a diffusion resistance (M_α) of 243 Ω with a higher time constant of 1.8 s, since the major contribution to the electrochemical behavior comes from surface-controlled processes, restricting the diffusion of ions to near-surface volume as suggested by the diffusion dispersion parameter (α) of 0.796.[59,63–65] Contrarily, the partially etched Mo_2AlB_2 shows higher diffusion contribution as inferred from the CV analyses and the resistive-like impedance response in the low frequency range, suggesting an anomalous mechanism of diffusion.[66] That being said, we model the equivalent circuit using a Bisquert element (M_γ) associated with the diffusion resistance of 524 Ω of the Mo_2AlB_2 material with faster kinetics as indicated by the time-constant of 0.8 s. The anomalous diffusion coefficient (γ) value of 0.186 further indicated anomalous heterogeneous transport processes within the electrode.[64–66]

To further understand the electrochemistry of the $Mo_{4/3}B_2T_x$ aerogel, the voltage profile at 200 mA g^{-1} across various cycle numbers (cycles 1–5, 20, 100, 200, and 500) is shown in Fig. 3c. The continuous sloping behavior observed across all cycles, along with the absence of well-defined plateaus, suggests that the electrochemical process follows a solid-solution reaction mechanism. In this mechanism, lithiation and de-lithiation occur gradually and continuously without the formation of distinct phase boundaries or significant structural transformations.[67] The inherent lack of sharp interfaces, due to the absence of two-phase transitions, minimizes mechanical stress on the electrode material,[68] thereby enhancing life-cycling stability.

Rate handling capability testing of $Mo_{4/3}B_2T_x$ aerogel was conducted. Results are shown in Fig. 3d, where specific capacities of 260 mAh g^{-1}, 230 mAh g^{-1}, 215 mAh g^{-1}, 200 mAh g^{-1}, 180 mAh g^{-1}, and 160 mAh g^{-1} were achieved at progressively increasing rates of 20 mA g^{-1}, 50 mA g^{-1}, 100 mA g^{-1}, 200 mA g^{-1}, 500 mA g^{-1}, and 1 A g^{-1}, respectively. The gradual capacity decay with rising specific current reflects kinetic limitations arising from sluggish Li-ion diffusion or charge-transfer resistance at elevated rates. Despite this trend, it retains more than 60% of its initial capacity (160 mAh g^{-1}) even at 1 A g^{-1}, demonstrating a balance between capacity retention and high-rate capability.

The stability during cycling of $Mo_{4/3}B_2T_x$ aerogel, shown in Fig. 3e, reveals remarkable activation behavior. The cycling stability was carried out at specific currents of 100 mA g^{-1}, 200 mA g^{-1}, 500 mA g^{-1}, 1000 mA g^{-1}, and 2000 mA g^{-1}. A gradual increase in specific capacity is observed across all specific currents. At 100 mA g^{-1} and 200 mA g^{-1}, the specific capacity exhibits a continuously increasing trend, which suggests improved Li-ion accessibility. At 500 mA g^{-1} and 1 A g^{-1}, a significant portion of specific capacity is retained. Even at the highest applied specific current of 2 A g^{-1}, the specific capacity is retained at 260 mAh g^{-1} after 500 cycles. To place this performance in context, previously reported multi-layered $Mo_{4/3}B_2T_x$ anodes delivered a specific capacity of 280 mAh g^{-1} after 100 cycles at a relatively low current density of 50 mA g^{-1}.[28] In comparison, the delaminated $Mo_{4/3}B_2T_x$ aerogel in this work maintains high capacity under much higher current densities and longer cycling, emphasizing the importance of delamination in improving high-rate electrochemical performance.

To evaluate practical performance, energy and power densities were extracted from discharge profiles. Under 100 mA g^{-1}, the aerogel delivers an energy density of 363 Wh kg^{-1} after 500 cycles. At 2 A g^{-1}, it achieves a power density of 1300 W kg^{-1} while sustaining 172 Wh kg^{-1}. These values compare favorably with other Mo-based systems. For example, MoS_2 electrodes typically provide 32 Wh kg^{-1} at 425 W kg^{-1},[69] while MoO_2 electrodes can reach 79 Wh kg^{-1} at 2450 W kg^{-1}.[70] Although Mo-based systems can extend to a higher maximum power output, they do so at the expense of energy density. By contrast, $Mo_{4/3}B_2T_x$ aerogel retains more than double the energy density at comparable power levels, positioning it as a strong candidate for applications requiring both high energy and stable power delivery.

This high performance can be attributed to its defect-tolerant architecture and solid-solution lithiation mechanism. The lack of phase boundaries effectively prevents stress accumulation, while the aerogel framework provides structural flexibility, accommodating volumetric changes and preventing mechanical failure. Furthermore, the Coulombic efficiency remains consistently above 95% throughout the cycling testing at such high specific current, confirming the ability to sustain prolonged cycling and reversibility without significant degradation. This combination of high-capacity retention, rate performance, and cycling reversibility positions the $Mo_{4/3}B_2T_x$ aerogel as a leading candidate for durable, high-power-density batteries and high-energy-density ionic capacitors.

3.3. DFT calculations

To better understand the stability of Li within $Mo_{4/3}B_2T_x$ and identify the most favorable positions for Li, the lithiation energy was calculated using DFT. In the present DFT calculations, an O-terminated $Mo_{4/3}B_2T_x$ surface was employed as a representative and simplified model for the MBene surface chemistry. Experimentally, TBAOH treatment is known to significantly reduce F terminations in MXenes, leading to surfaces predominantly terminated with O and OH groups;[71,72] a similar behavior is expected for MBenes. However, the experimentally obtained MBene surface likely consists of mixed terminations, and explicitly modeling such a complex termination environment would significantly complicate the calculations. Therefore, the O-terminated model was chosen to capture the dominant trends in Li-ion adsorption and diffusion and to provide qualitative insight into favorable intercalation

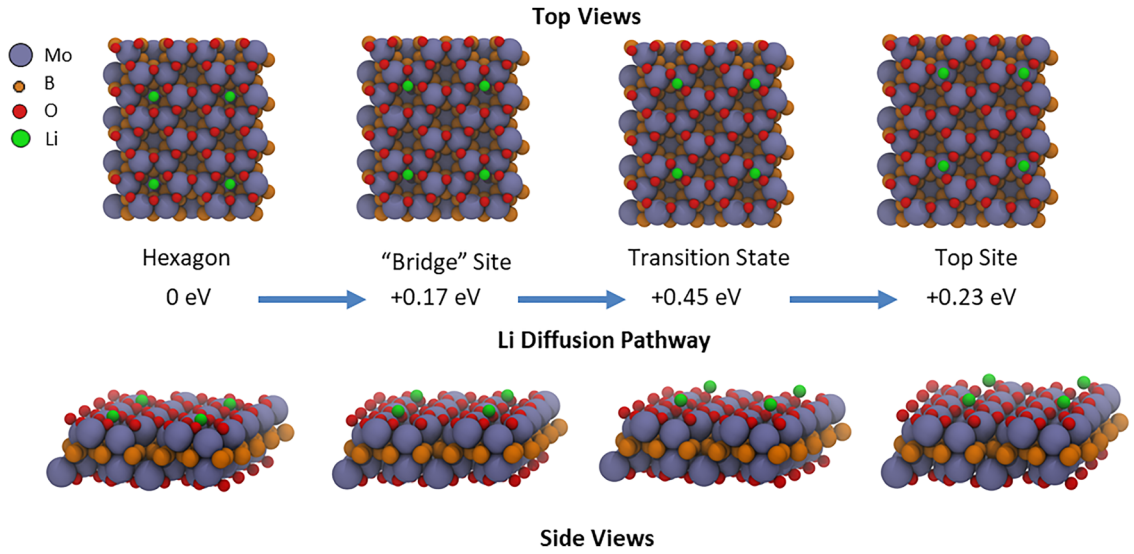

Fig. 4 DFT-calculated relative energies for Li positions in $Mo_{4/3}B_2O_2$ referenced to the lowest energy geometry. Half of the diffusion pathway is shown, as the other half is symmetry-equivalent.

sites, rather than to exactly replicate the experimental surface termination chemistry. The lattice constants for $Mo_{4/3}B_2T_x$ and Li are listed in SI, Table S2. Fig. 4 illustrates the diffusion path geometries for Li, along with the corresponding calculated relative energies, giving a total diffusion barrier of 0.45 eV. A single Li atom was positioned in four distinct sites: on top of a Mo atom, at a Mo–Mo bridge site, at a transition state, and within the hexagonal Mo ring (hexagon). Among these four positions, Li located in the hexagon exhibited the highest intercalation potential, as indicated by its most negative intercalation energy value of −2.74 eV. Additionally, Fig. 4 presents the relative energies for each position, while the detailed calculated intercalation energies are provided in SI, Table S3.

4. Conclusions

In this work, we demonstrated the successful synthesis, structural characterization, and electrochemical evaluation of a delaminated $Mo_{4/3}B_2T_x$ *i*-MBene aerogel derived from the *i*-MAB phase $Mo_{4/3}Y_{2/3}AlB_2$. The resulting 2D architecture exhibits more accessible active sites for Li storage and a defect-tolerant morphology, enabling both efficient ion transport and mechanical stability under extensive cycling. The $Mo_{4/3}B_2T_x$ aerogel exhibits high performance as an anode material for LIBs, featuring a high specific capacity, excellent rate handling capability, and long-term cycling stability. Specifically, a capacity of 260 mAh g^{-1} was achieved at 20 mA g^{-1}, and 260 mAh g^{-1} was retained even after 500 cycles at 2 A g^{-1}. At a moderate specific current of 100 mA g^{-1}, the electrode achieved an energy density of ∼363 Wh kg^{-1}. At 2 A g^{-1}, the material delivered 1300 W kg^{-1}, which compares favorably with state-of-the-art MoO_2-based and MoS_2-based systems. Electrochemical analyses, including CV and PEIS, revealed that pseudocapacitive processes with limited and restricted diffusion constraints dominate the charge storage mechanism. At the same time, the observed solid-solution behavior supports its long-term cycling durability. Complementary DFT calculations identified energetically favorable Li intercalation sites within the Mo lattice, with low diffusion barriers that underpin the observed high-rate performance.

Taken together, these results position $Mo_{4/3}B_2T_x$ *i*-MBene aerogels as a highly promising class of 2D electrode materials for high-power LIBs and hybrid LICs, offering a compelling combination of energy density, rate performance, and structural robustness for next-generation energy storage systems.

Author contributions

Karamullah Eisawi: methodology, investigation, data curation, validation, writing – original draft. Connor J Herring: investigation, formal analysis, data curation, writing – review & editing. Jean Gustavo de Andrade Ruthes: data curation, formal analysis, review & editing. Volker Presser: writing – review and editing. Matthew M Montemore: supervision, writing – review and editing. Michael Naguib: supervision, funding acquisition, conceptualization, writing – review and editing.

Conflicts of interest

The authors have no conflict of interest.

Data availability

All data supporting the findings of this study are available from the corresponding author upon reasonable request.

Supplementary information (SI): Table S1: Elemental composition of $Mo_{4/3}Y_{2/3}AlB_2$ *i*-MAB phase and $Mo_{4/3}B_2T_x$ *i*-MBene aerogel as determined by energy-dispersive spectroscopy (EDS). Fig. S1: ATR-FTIR spectra for $Mo_{4/3}Y_{2/3}AlB_2$, $Mo_{4/3}B_2T_x$ *i*-MBene

multilayered, TBAOH delaminated $Mo_{4/3}B_2T_x$ aerogel and LiCl treated $Mo_{4/3}B_2T_x$ aerogel. Fig. S2. Raman spectra for $Mo_{4/3}Y_{2/3}AlB_2$, $Mo_{4/3}B_2T_x$ *i*-MBene multilayered, TBAOH delaminated $Mo_{4/3}B_2T_x$ aerogel and LiCl treated $Mo_{4/3}B_2T_x$ aerogel. Table S2: Calculated lattice parameters for Li bulk and $Mo_{4/3}B_2$ and comparison to previous calculations. Table S3: Li intercalation energy values for $Mo_{4/3}B_2O_2$. Table S4: Equivalent circuit fitting of PEIS analysis of Mo_2AlB_2 and $Mo_{4/3}B_2T_x$. See DOI: https://doi.org/10.1039/d5ya00295h.

Acknowledgements

Materials synthesis, characterization, and electrochemical testing were supported by the National Science Foundation under Grant No. DMR-2048164. M. N. acknowledges support from the Alexander von Humboldt Foundation through the Humboldt Research Award. C. H. acknowledges support from the U.S.–Israel Center for Fossil Fuels, administered by the BIRD Foundation, and M. M. M. was supported by the National Science Foundation under Grant No. CHE-2154952. Tulane University is also acknowledged for support, in part through high-performance computing (HPC) resources provided by Technology Services, as well as HPC resources provided by the Louisiana Optical Network Infrastructure (https://www.loni.org).

References

1 L. Wang, Q. Zhang, J. Liu and G. Wang, *J. Energy Storage*, 2024, **77**, 109819.
2 J. B. Goodenough and K. S. Park, *J. Am. Chem. Soc.*, 2013, **135**, 1167–1176.
3 S. Orangi, N. Manjong, D. P. Clos, L. Usai, O. S. Burheim and A. H. Strømman, *J. Energy Storage*, 2024, **76**, 143934.
4 J. Li, Z. Du, R. E. Ruther, S. J. An, L. A. David, K. Hays, M. Wood, N. D. Phillip, Y. Sheng, C. Mao, S. Kalnaus, C. Daniel and D. L. Wood, *JOM*, 2017, **69**, 1484–1496.
5 J. Xu, X. Cai, S. Cai, Y. Shao, C. Hu, S. Lu and S. Ding, *Energy Environ. Mater.*, 2023, **6**, e12450.
6 W. He, W. Guo, H. Wu, L. Lin, Q. Liu, X. Han, Q. Xie, P. Liu, H. Zheng, L. Wang, X. Yu and D. L. Peng, *Adv. Mater.*, 2021, **33**, e2005937.
7 G. G. Amatucci, F. Badway, A. Du Pasquier and T. Zheng, *J. Electrochem. Soc.*, 2001, **148**, A930.
8 D. P. Dubal, O. Ayyad, V. Ruiz and P. Gomez-Romero, *Chem. Soc. Rev.*, 2015, **44**, 1777–1790.
9 A. Jagadale, X. Zhou, R. Xiong, D. P. Dubal, J. Xu and S. Yang, *Energy Storage Mater.*, 2019, **19**, 314–329.
10 J. Liu and X. W. Liu, *Adv. Mater.*, 2012, **24**, 4097–4111.
11 R. Rojaee and R. Shahbazian-Yassar, *ACS Nano*, 2020, **14**, 2628–2658.
12 K.-S. Chen, I. Balla, N. S. Luu and M. C. Hersam, *ACS Energy Lett.*, 2017, **2**, 2026–2034.
13 M. Naguib, M. W. Barsoum and Y. Gogotsi, *Adv. Mater.*, 2021, **33**, e2103393.
14 C. Qiao, H. Wu, X. Xu, Z. Guan and W. Ou-Yang, *Adv. Mater. Interfaces*, 2021, **8**, 2100903.
15 L. Jia, S. Zhou, A. Ahmed, Z. Yang, S. Liu, H. Wang, F. Li, M. Zhang, Y. Zhang and L. Sun, *Chem. Eng. J.*, 2023, **475**, 146361.
16 H. Chen, H. Ma and C. Li, *ACS Nano*, 2021, **15**, 15502–15537.
17 M. Li, Q. Fan, L. Gao, K. Liang and Q. Huang, *Adv. Mater.*, 2024, e2312918, DOI: 10.1002/adma.202312918.
18 K. Liang, R. A. Matsumoto, W. Zhao, N. C. Osti, I. Popov, B. P. Thapaliya, S. Fleischmann, S. Misra, K. Prenger, M. Tyagi, E. Mamontov, V. Augustyn, R. R. Unocic, A. P. Sokolov, S. Dai, P. T. Cummings and M. Naguib, *Adv. Funct. Mater.*, 2021, **31**, 2104007.
19 V. Natu and M. W. Barsoum, *J. Phys. Chem. C*, 2023, **127**, 20197–20206.
20 M. Jiang, D. Wang, Y. H. Kim, C. Duan, D. V. Talapin and C. Zhou, *Angew. Chem., Int. Ed.*, 2024, **63**, e202409480.
21 D. Bury, M. Jakubczak, M. A. K. Purbayanto, M. Rybak, M. Birowska, A. Wójcik, D. Moszczyńska, K. Eisawi, K. Prenger, V. Presser, M. Naguib and A. M. Jastrzębska, *Adv. Funct. Mater.*, 2023, **33**, 2308156.
22 Y. Yang, H. Wang, C. Wang, J. Liu, H. Wu, N. Liu, Q. Wang, Y. Shang and J. Zheng, *Small*, 2024, **20**, e2405870.
23 Z. Guo, J. Zhou and Z. Sun, *J. Mater. Chem. A*, 2017, **5**, 23530–23535.
24 S. Ahmad, H. Xu, L. Chen, H. U. Din and Z. Zhou, *Nanotechnology*, 2024, **35**, 285401.
25 J. Wang, L. Bai, X. Zhao, H. Gao and L. Niu, *RSC Adv.*, 2022, **12**, 28525–28532.
26 A. Majed, M. Torkamanzadeh, C. F. Nwaokorie, K. Eisawi, C. Dun, A. Buck, J. J. Urban, M. M. Montemore, V. Presser and M. Naguib, *Small Methods*, 2023, **7**, e2300193.
27 J. Zhou, J. Palisaitis, J. Halim, M. Dahlqvist, Q. Tao, I. Persson, L. Hultman, P. O. A. Persson and J. Rosen, *Science*, 2021, **373**, 801–805.
28 M. U. Khan, L. Du, X. San, Y. Zhou, M. Jiang, L. Chu, Q. Feng and C. Hu, *J. Appl. Electrochem.*, 2025, 1721–1730.
29 G. Liu, W. Yuan, Z. Zhao, J. Li, N. Wu, D. Guo, X. Liu, Y. Liu, A. Cao and X. Liu, *Chem. Eng. J.*, 2024, **493**, 152576.
30 Z. Zhang, W. Ling, N. Ma, J. Wang, X. Chen, J. Fan, M. Yu and Y. Huang, *Adv. Funct. Mater.*, 2023, **34**, 2310294.
31 P. Liu, H. Xu, X. Wang, G. Tian, X. Yu, C. Wang, C. Zeng, S. Wang, F. Fan, S. Liu and C. Shu, *Small*, 2024, **20**, e2404483.
32 K. Matthews, T. Zhang, C. E. Shuck, A. VahidMohammadi and Y. Gogotsi, *Chem. Mater.*, 2021, **34**, 499–509.
33 G. Kresse, *J. Non-Cryst. Solids*, 1995, **192–193**, 222–229.
34 G. Kresse and J. Furthmüller, *Comput. Mater. Sci.*, 1996, **6**, 15–50.
35 J. P. Perdew, K. Burke and M. Ernzerhof, *Phys. Rev. Lett.*, 1996, **77**, 3865–3868.
36 P. Helmer, J. Halim, J. Zhou, R. Mohan, B. Wickman, J. Björk and J. Rosen, *Adv. Funct. Mater.*, 2022, **32**, 2109060.
37 A. Heyden, A. T. Bell and F. J. Keil, *J. Chem. Phys.*, 2005, **123**, 224101.
38 M. Naguib, O. Mashtalir, J. Carle, V. Presser, J. Lu, L. Hultman, Y. Gogotsi and M. W. Barsoum, *ACS Nano*, 2012, **6**, 1322–1331.

39 N. B. Asanbaeva, D. A. Rychkov, P. Y. Tyapkin, S. G. Arkhipov and N. F. Uvarov, *Struct. Chem.*, 2021, **32**, 1261–1267.
40 A. L. James and K. Jasuja, *RSC Adv.*, 2017, **7**, 1905–1914.
41 K. Zielinkiewicz, D. Baranowska and E. Mijowska, *RSC Adv.*, 2023, **13**, 16907–16914.
42 S. Güngör, C. Taşaltın, İ. Gürol, G. Baytemir, S. Karakuş and N. Taşaltın, *Appl. Phys. A:Mater. Sci. Process.*, 2022, **128**, 89.
43 A. Kumar, S. B. Rai and D. K. Rai, *Mater. Res. Bull.*, 2003, **38**, 333–339.
44 A. Haydar, *Int. J. Math., Phys. Eng. Sci.*, 2012, **7**, 922–926.
45 X.-Y. Li, J. Yan, D.-L. Zhong, S.-J. Lu and B.-B. Ge, *Ind. Eng. Chem. Res.*, 2023, **62**, 2504–2515.
46 S. Sheng, J.-B. Wu, X. Cong, Q. Zhong, W. Li, W. Hu, J. Gou, P. Cheng, P.-H. Tan, L. Chen and K. Wu, *ACS Nano*, 2019, **13**, 4133–4139.
47 S. Vinoth, H. T. Das, M. Govindasamy, S.-F. Wang, N. S. Alkadhi and M. Ouladsmane, *J. Alloys Compd.*, 2021, **877**, 160192.
48 Y. Wang, G. Wang, Y. Wang, L. Zhou, J. Kang, W. Zheng, S. Xiao, G. Xing and J. He, *J. Phys. Chem. Lett.*, 2024, **15**, 3461–3469.
49 N. Elgrishi, K. J. Rountree, B. D. McCarthy, E. S. Rountree, T. T. Eisenhart and J. L. Dempsey, *J. Chem. Educ.*, 2017, **95**, 197–206.
50 C. Sandford, M. A. Edwards, K. J. Klunder, D. P. Hickey, M. Li, K. Barman, M. S. Sigman, H. S. White and S. D. Minteer, *Chem. Sci.*, 2019, **10**, 6404–6422.
51 V. Augustyn, E. R. White, J. Ko, G. Grüner, B. C. Regan and B. Dunn, *Mater. Horiz.*, 2014, **1**, 219–223.
52 H. Lindström, S. Södergren, A. Solbrand, H. Rensmo, J. Hjelm, A. Hagfeldt and S.-E. Lindquist, *J. Phys. Chem. B*, 1997, **101**, 7717–7722.
53 Y. Jiang and J. Liu, *Energy Environ. Mater.*, 2019, **2**, 30–37.
54 S. J. Panchu, K. Raju and H. C. Swart, *ChemElectroChem*, 2024, **11**, e202300810.
55 H. D. Yoo, Y. Li, Y. Liang, Y. Lan, F. Wang and Y. Yao, *ChemNanoMat*, 2016, **2**, 688–691.
56 A. Majed, M. Torkamanzadeh, C. F. Nwaokorie, K. Eisawi, C. Dun, A. Buck, J. J. Urban, M. M. Montemore, V. Presser and M. Naguib, *Small Methods*, 2023, **7**, 2300193.
57 G. K. Sharma, J. Elkins, A. B. Puthirath, J. Murukeshan, A. Biswas, T. S. Pieshkov, A. Pramanik, R. Vajtai, D. Kaur and P. M. Ajayan, *Small*, 2025, **21**, e2500361.
58 H. Wu, Z. Guo, J. Zhou and Z. Sun, *Appl. Surf. Sci.*, 2019, **488**, 578–585.
59 P. Ryś, J. Kowalczyk, M. Mroczkowska-Szerszeń, M. Kaczkan, P. Moszczyński, W. Pudełko and M. Siekierski, *Appl. Phys. A: Mater. Sci. Process.*, 2024, **130**, 797.
60 Y. T. Malik, M. Braig, P. Simon, R. Zeis and S. Fleischmann, *J. Electrochem. Soc.*, 2024, **171**, 110515.
61 M. Y. Perdana, B. A. Johan, M. Abdallah, M. E. Hossain, M. A. Aziz, T. N. Baroud and Q. A. Drmosh, *Chem. Rec.*, 2024, **24**, e202400007.
62 A. Lasia, *J. Phys. Chem. Lett.*, 2022, **13**, 580–589.
63 V. Augustyn, P. Simon and B. Dunn, *Energy Environ. Sci.*, 2014, **7**, 1597–1614.
64 Z. Zeng, B.-A. Mei, G. Song, M. Hamza, Z. Yan, Q. Wei, H. Feng, Z. Zuo, B. Jia and R. Xiong, *J. Energy Storage*, 2024, **102**, 114021.
65 J. P. Diard and C. Montella, *J. Electroanal. Chem.*, 2003, **557**, 19–36.
66 J. Bisquert and A. Compte, *J. Electroanal. Chem.*, 2001, **499**, 112–120.
67 A. R. Armstrong, G. Armstrong, J. Canales and P. G. Bruce, *J. Power Sources*, 2005, **146**, 501–506.
68 L. S. de Vasconcelos, R. Xu, Z. Xu, J. Zhang, N. Sharma, S. R. Shah, J. Han, X. He, X. Wu, H. Sun, S. Hu, M. Perrin, X. Wang, Y. Liu, F. Lin, Y. Cui and K. Zhao, *Chem. Rev.*, 2022, **122**, 13043–13107.
69 S. Wei, R. Zhou and G. Wang, *ACS Omega*, 2019, **4**, 15780–15788.
70 M. Lathika Divya, Y.-S. Lee and V. Aravindan, *Phys. Rev. Appl.*, 2023, **19**, 034016.
71 M. Naguib, R. R. Unocic, B. L. Armstrong and J. Nanda, *Dalton Trans.*, 2015, **44**, 9353–9358.
72 K. Liang, A. Tabassum, M. Kothakonda, X. Zhang, R. Zhang, B. Kenney, B. D. Koplitz, J. Sun and M. Naguib, *Mater. Rep.: Energy*, 2022, **2**, 100075.